Article

Graphene-Oxide-Coated CoP2@C Anode Enables High Capacity of Lithium-Ion Batteries

Wei Zhang [1], Hangxuan Xie [1], Zirui Dou [1], Zhentao Hao [1], Qianhui Huang [1], Ziqi Guo [1], Chao Wang [1], Kanghua Miao [2],* and Xiongwu Kang [2],*

[1] China Southern Power Grid Technology Co., Ltd., Guangzhou 510080, China
[2] New Energy Research Institute, School of Environment and Energy, South China University of Technology, Guangzhou 510006, China
* Correspondence: huakm11@163.com (K.M.); esxkang@scut.edu.cn (X.K.)

Abstract: Cobalt diphosphides (CoP_2) show a high theoretical capacity and hold great promise as anode materials for lithium-ion batteries (LIBs). However, the large variation in the volume and structure of CoP_2 caused during lithium-ion insertion and extraction results in electrode fragmentation and a compromised solid electrolyte interface, ultimately leading to poor cycling performance. Herein, a composite of CoP_2 nanoparticles encapsulated in carbon matrix has been successfully synthesized by carbonization of Co-MOF-based zeolitic imidazolate frameworks (ZIF-67) and sequential phosphorization and further wrapped in graphene oxide ($CoP_2@C@GO$). The formation of CoP_2 was confirmed by X-ray diffraction, high-resolution transmission electron microscopy and X-ray photoelectron spectroscopy. The morphology of $CoP_2@C$ with and without GO wrapping was examined by scanning electron microscopy and transmission electron spectroscopy. It was demonstrated that the decoration of GO significantly reduces the polarization of $CoP_2@C$ electrodes, enhancing their charge capacity and cycling stability as an anode material for LIBs. After 200 cycles, they deliver a capacity of 450 mAh·g^{-1}.

Keywords: cobalt diphosphides; ZIF-67; phosphorization; structure integrity; stabilization

1. Introduction

Lithium-ion batteries (LIBs) are widely used in portable electronics and electric vehicles. Currently, commercial graphite is the primary anode material used in LIBs. However, the slow kinetics of Li$^+$ intercalation and low theoretical specific capacity result in mileage anxiety for electric vehicles [1,2]. Thus, there is an increasing demand for advanced anode materials in LIBs with long cycle lifespan, high capacity and superior rate performance. Hard carbon, owing to a large number of microporous structures, layered structures with a larger spacing than graphite layers, enables fast lithium-ion inversion and extraction and holds great promise in rate performance, thus it is considered another type of anode material for LIBs [3].

Transition metal phosphides are considered alternative anode materials for LIBs due to their high gravimetric and volumetric capacities (500−1800 mAh·g^{-1}). In the early studies of transition metal phosphides as anode materials, their performance was relatively poor, and research primarily focused on exploring the reaction mechanisms, which strongly depend on the type of transition metal within the metal phosphides. For instance, a teardrop-shaped $SnP_{0.94}$ was prepared by reaction of tin acetate in a solution of trioctyl phosphine and triocylphosphine oxide and exhibited a reversible capacity of 740 mAh·g^{-1} [4] in the potential range of 0 to 1.2 V. The structural transformation of $SnP_{0.94}$ during the charging/discharging process indicates a fully reversible and purely lithium intercalation reaction process, without any metallization reaction. The electrochemical performance of such nanosized $SnP_{0.94}$ surpasses that of Sn_4P_3 prepared using the traditional solid-state reaction method based on tin and red phosphorus.

In another study in 2009, the reaction mechanism of lithiation reaction of crystalline FeP, FeP_2 and FeP_4 as anode materials of LIBs was explored by Mossbauer spectroscopy, magnetic characterization and nuclear magnetic resonance (NMR) spectroscopy [5]. Interestingly, it was found that electrochemical reaction of FeP and FeP_2 with Li ions leads to full or partial conversion to Li_3P and Fe, accompanied with a reaction intermediate phase of FeP and LiFeP. In contrast, FeP_4 only exhibits an insertion mechanism as identified for transition metal phosphides of titanium, vanadium, manganese and tin [4], and no conversion reaction products of Li_3P and Fe were identified at all. Usually, it is considered that the conversion of Li_3P to LiP at potentials higher than 0.65 V may result in rapid capacity decay due to the much poorer electronic conductivity of LiP than Li_3P [4]. Thus, the formation of Li_3P in lithiation of FeP favors the longevity of FeP anode materials in LIBs. In the following study, an amorphous iron diphosphide (FeP_2) [6] was obtained by reaction of $Fe(N(SiMe_3)_2)_3$ with phosphine (PH_3) in tetrahydrofuran (THF) at a low temperature of 100 °C, which exhibited extremely high discharge and charge capacity of 1258 and 766 mAh·g^{-1} as anode materials of LIBs. However, the cycling is limited to only 10 cycles.

Many other transition metal phosphides, such as ZnP_2 [7], Ni_3P [8], Ni_2P [9,10] and CuP_2 [11], have been reported. As to phosphorus-rich CuP_2 embedded in carbon matrix [11], irreversible reactions between CuP_2 and lithium were observed. Cu_3P and amorphous phosphorus were reversibly formed in the first discharging process and subsequent cycles. It was demonstrated that the carbon content is also a significant factor in regulating the capacity of LIBs in terms of offering high electronic conductivity, fast reaction kinetics and structural integrity of the anode.

Cobalt phosphides are important anode materials, which have equally been well explored. For instance, CoP and Co_2P binary compounds were prepared by a simple solid-state reaction method and the lithiation mechanism was explored by a combination of X-ray diffraction (XRD) and extended X-ray absorption fine structure [12]. It was claimed that lithiation of CoP is possible but Co_2P does not react with lithium or contribute to the capacity of the LIBs. Many investigations of anodes of CoP can be found in the literature, such as CoP/C modified with MCNTs [13], hierarchical porous CoP/C nanoboxes [14], CoP thin film [15], CoP nanoparticles encapsulated in coralloidal carbon [16], CoP nanoparticles wrapped in N-doped CNTs [17] and peapod-like CoP hollow nanorods [18].

Porous CoP_3 microcubes [19] were derived from the reaction of cubic $Co_3[Co(CN)_6]_2$ particles by a modified co-precipitation method with red phosphorus and subsequently coated with polypyrrole (PPy). The conducting PPy layer is considered a buffer layer, which alleviates the large volumetric variation and promotes charge transfer kinetics during the lithiation/delithiation process. CoP [20] exhibits relatively low charge and discharge voltage plateaus, which are 0.9 and 0.6 V, respectively, rendering it a suitable anode material for secondary batteries. However, there is limited literature regarding the synthesis, structural engineering and application of CoP_2 in energy storage for LIBs [21].

It is concluded that Li-ion storage in transition metal phosphides can be mainly divided into two types [22,23]: (i) insertion mechanism and (ii) conversion mechanism, as described in Equations (1) and (2), respectively.

$$M_xP_y + zLi \rightarrow Li_zM_xP_y \tag{1}$$

$$M_xP_y + 3Li \rightarrow yLi_3P + xM \tag{2}$$

During the insertion and extraction reaction of Li ions in electrode materials, the large volumetric variation may result in mechanical strength, morphology evolution [24] and even fragmentation of the electrode materials and re-construction of the solid–electrolyte interface layer [25], which causes fast decay of the capacity of the batteries. Additionally, the poor electronic conductivity of Li_3P and LiP formed during the discharging process is also an obstacle for the high capacity and long cycling performance of LIBs [4]. Thus, it is desirable to develop strategies to stabilize the nanostructure of the electrode materials,

constrain the solid–electrolyte interface layer and maintain the high electronic conductivity of the anode materials of metal phosphides [26].

Numerous strategies have been developed to improve the electrochemical performance of the anode materials of LIBs. For instance, preparing porous carbon-supported transition metal nanoparticles [27], sulfides and selenides [28–30] by using a metal organic framework as a template and self-supported phosphide nanorod arrays [31] shows great potential in obtaining high-performance anode materials of LIBs, sodium ion batteries and even lithium sulfur batteries. Graphene or graphene oxide, as a single-layered 2D carbon sheet, shows high conductivity and chemical and mechanical stability and has been widely applied in proving energy storage performances [32]. Combining active electrode materials with graphene has also achieved great success in improving the electrode performance for batteries [33]. Nanostructure engineering, such as making yolk–shell structures [34], hollow structures and open frameworks [35,36], shows great promise in improving the charge capacity and cycling performance of electrode materials for LIBs.

Inspired by previous work on designing high-performance nanomaterials for electrochemical energy storage performance, in this manuscript, CoP_2@C derived from a Co-MOF-based zeolitic imidazolate framework (ZIF-67) was wrapped with graphene oxide (GO). SEM and TEM analysis revealed that the cubic CoP_2@C nanoparticles were completely enveloped by GO. The decoration of GO on CoP_2@C in CoP_2@C@GO enables a reversible capacity of 452 mAh·g^{-1} after 200 charge/discharge cycles at the current rate of 1 A·g^{-1}.

2. Results

Figure S1A,B are SEM images of ZIF-67. After the carbonization and phosphorization of ZIF-67, CoP_2@C nanoparticles were obtained. The morphology of CoP_2@C and CoP_2@C@GO samples was examined by SEM and TEM measurements, as shown in Figure 1. It is observed that CoP_2@C nanoparticles distribute uniformly, with a smooth surface and diameter of about 50 nm (Figure 1A,D). TEM images of CoP_2@C@GO (Figure 1B,E) indicate that CoP_2@C nanoparticles were covered by GO sheets. The lattice fringes with an interspacing distance of 2.50 Å corresponded to (200) planes of orthorhombic CoP_2 (Figure 1C,F).
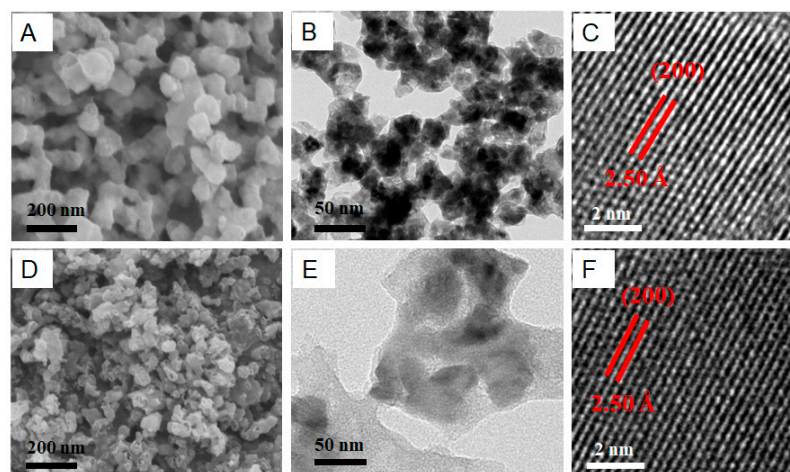

Figure 1. (**A**) SEM and (**B**) TEM images of CoP_2@C. (**D**) SEM and (**E**) TEM images of CoP_2@C@GO. HRTEM and lattice stripe of CoP_2 (200) in (**C**) CoP_2@C and (**F**) CoP_2@C@GO.

The XRD pattern of the synthesized ZIF-67 is shown in Figure 2A, which is consistent with the simulated spectrum, indicating the high purity of the synthesized ZIF-67 [26]. Figure 2B shows the XRD pattern of CoP_2@C after carbonization of ZIF-67, which is in agreement with the standard JCPDS card No. 26-0481, suggesting the successful preparation of pyrite CoP_2. According to the diffraction peak at $2\theta = 35.6°$, the interspacing of the (200)

crystalline plane of CoP_2 in $CoP_2@C$ was determined to be 2.51 Å, in accordance with that obtained from HRTEM and shown in Figure 1C,F.
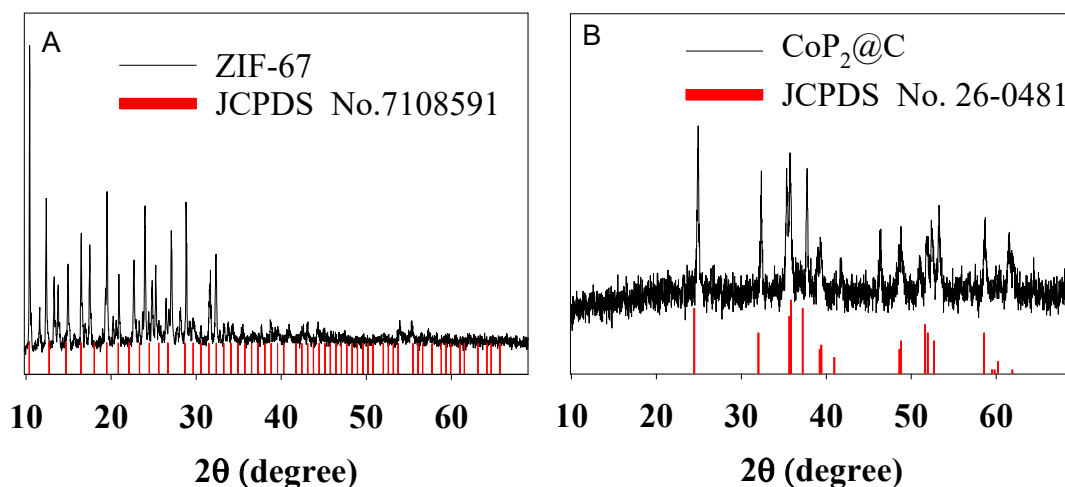

Figure 2. XRD patterns of (**A**) ZIF-67 and (**B**) $CoP_2@C$.

Figures 3A and S2A display survey XPS of $CoP_2@C$ and $CoP_2@C@GO$, where Co, P, C, O and N elements were observed. The high-resolution N 1s XPS was deconvoluted into three peaks, which were indexed to graphitic N (401.2 eV), pyrrolic N (400.1 eV) and pyridinic N (399.7 eV) [37], respectively, as shown in Figure 3B. Figure 3C shows the high-resolution Co 2p XPS of $CoP_2@C@GO$. The peaks at 778.8 and 795.4 eV are assigned to Co $2p^{3/2}$ and $2p^{1/2}$ in CoP_2 [38], which are well consistent with the result of XRD patterns in Figure 2B.

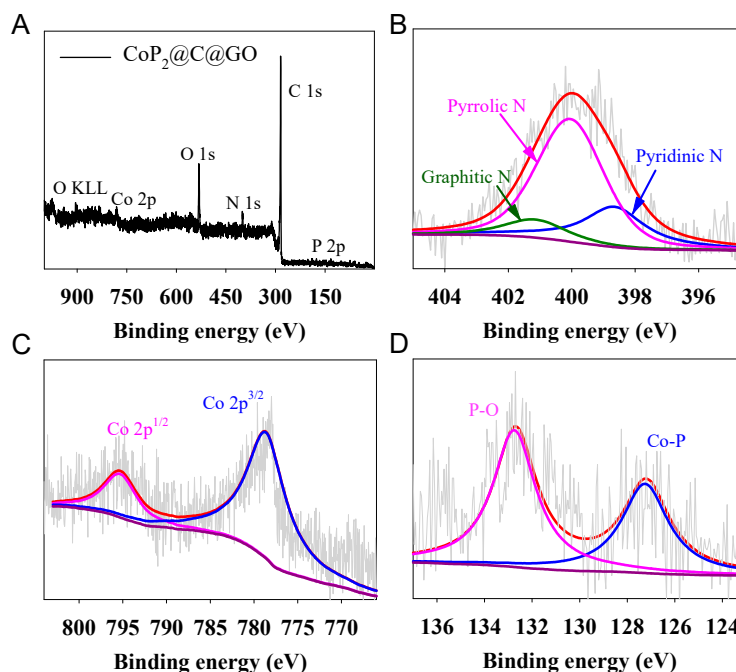**Figure 3.** (**A**) Survey and high-resolution XPS, (**B**) N 1s, (**C**) Co 2p, (**D**) P 2p of $CoP_2@C@GO$.

The XPS results of P 2p are shown in Figure 3D, which were deconvoluted into two peaks. The peak at 127.1 eV is ascribed to the P 2p of CoP_2, indicating the successful phosphorization of cobalt, while the other peak at 132.8 eV was indexed to the partial oxidation of CoP_2 upon exposure to the air [39]. It should be noted that the binding energy of Co $2p^{3/2}$ and $2p^{1/2}$ in $CoP_2@C$ is observed at 781.2 and 798.5 eV and the binding

energy of P 2p in CoP_2@C is 129.6 eV (Figure S2) [40], which are much higher than that of CoP_2@C@GO. This indicates that decoration of GO on CoP_2@C induces a significant red-shift of the binding energy for both P and Co of CoP_2 in CoP_2@C@GO. The lowered binding energy and the weakened intensity of Co 2p and P 2p XPS peaks in CoP_2@C@GO relative to those of CoP_2@C are ascribed to the van der Waals interaction between CoP_2 and GO and the electronic screening effect of GO [41].

The electrochemical performance of the CoP_2@C and CoP_2@C@GO composites as anodes of rechargeable LIBs was explored in 2016-type coin cells. The initial three CV curves were acquired for anodes of CoP_2@C and CoP_2@C@GO in the potential window of 0.0 to 3.0 V vs. Li^+/Li at a scan rate of 0.1 mV s^{-1}, as shown in Figure 4A. The first reduction peak at 0.523 V is related to Li^+ insertion into the CoP_2@C forming Li_xCoP_2 and further to Co and Li_3P, which was shifted to 0.618 V for CoP_2@C@GO. The second reduction peak around 0.01 V is attributed to the conversion of Li ions into carbon materials [42], which is increased to 0.173 V. The oxidization peak around 1.217 V for CoP_2@C is associated with Co and Li_3P oxidation to CoP_2 [43], which is almost identical for both CoP_2@C and CoP_2@C@GO. This indicates much reduced polarization for the CoP_2@C anode upon GO decoration due to the enhanced electronic conductivity and the electronic screening effect.

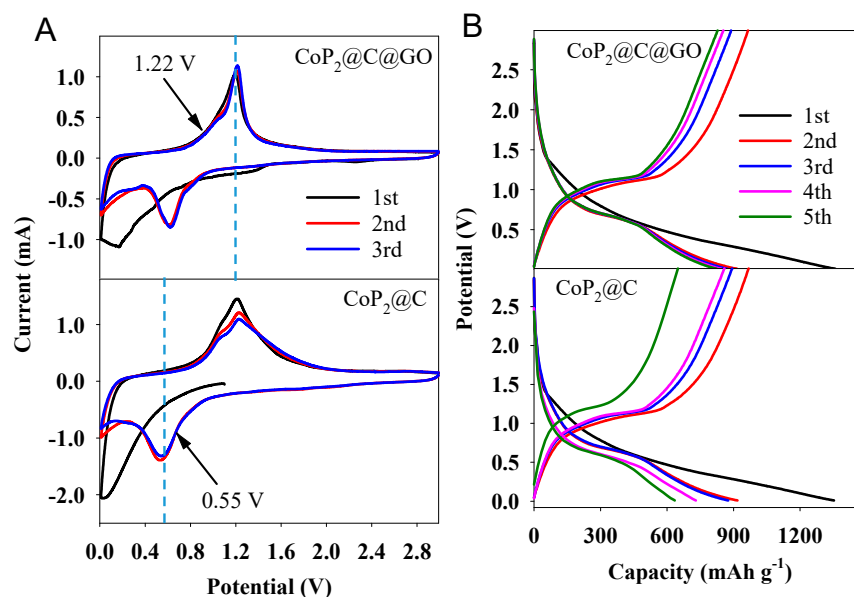**Figure 4.** (**A**) CV curves at a scan rate of 0.1 mV s^{-1} in the voltage range of 3.0–0 V vs. Li/Li^+ and (**B**) galvanostatic discharge and charge curves at 0.5 C for CoP_2@C and CoP_2@C@GO, respectively.

Figure 4B displays the voltage–capacity curves of CoP_2 at 1 A·g^{-1} in the first five cycles. The voltage–capacity curves in the initial charge/discharge cycle show two plateaus at around 1.22 and 0.618 V, respectively, in accordance with the redox peaks in the 1st cyclic voltammetry (CV) curve in Figure 4A. It is observed that the initial discharge capacity of LIBs reaches about 1450 mAh·g^{-1} for CoP_2@C@GO and 1347 mAh·g^{-1} for CoP_2@C@GO and a high reversible charge capacity of 1026 and 964 mAh·g^{-1} for CoP_2@C@GO and CoP_2@C, respectively. The delivered initial Coulombic efficiency is 71% for CoP_2@C@GO and 72% for CoP_2@C, which are close to each other. The last four discharge curves overlap with each other very well for CoP_2@C@GO, indicating much-enhanced cycling performance upon GO decoration.

As shown in Figure 5A, CoP_2@C@GO exhibits a much-enhanced rate capability compared to the as-prepared CoP_2@C. At a rate of 0.05 A g^{-1}, the initial discharge capacity is up to 1210 mAh·g^{-1}, which is superior to that of the CoP nanorod array counterpart [30] and free-standing CoP_2 nanosheets coated with hierarchical carbon [36]. The subsequent decline of specific capacity is ascribed to the activation process [44]. The specific capacity gradually degenerates as the current rate increases from 0.05 to 2 A g^{-1}. The reversible

capacity of 705, 638, 564 and 460 mAh$\cdot$g^{-1} at a current density of 0.1, 0.5, 1 and 2 A g^{-1}, respectively, was retained [20]. This is equally superior to that of the CoP [30,45] and free-standing CoP$_2$ nanosheets [36] reported in the literature. When the current density is returned to 0.05 A g^{-1}, most of its specific capacity was recovered and retained a value of 705 mAh$\cdot$g^{-1}.
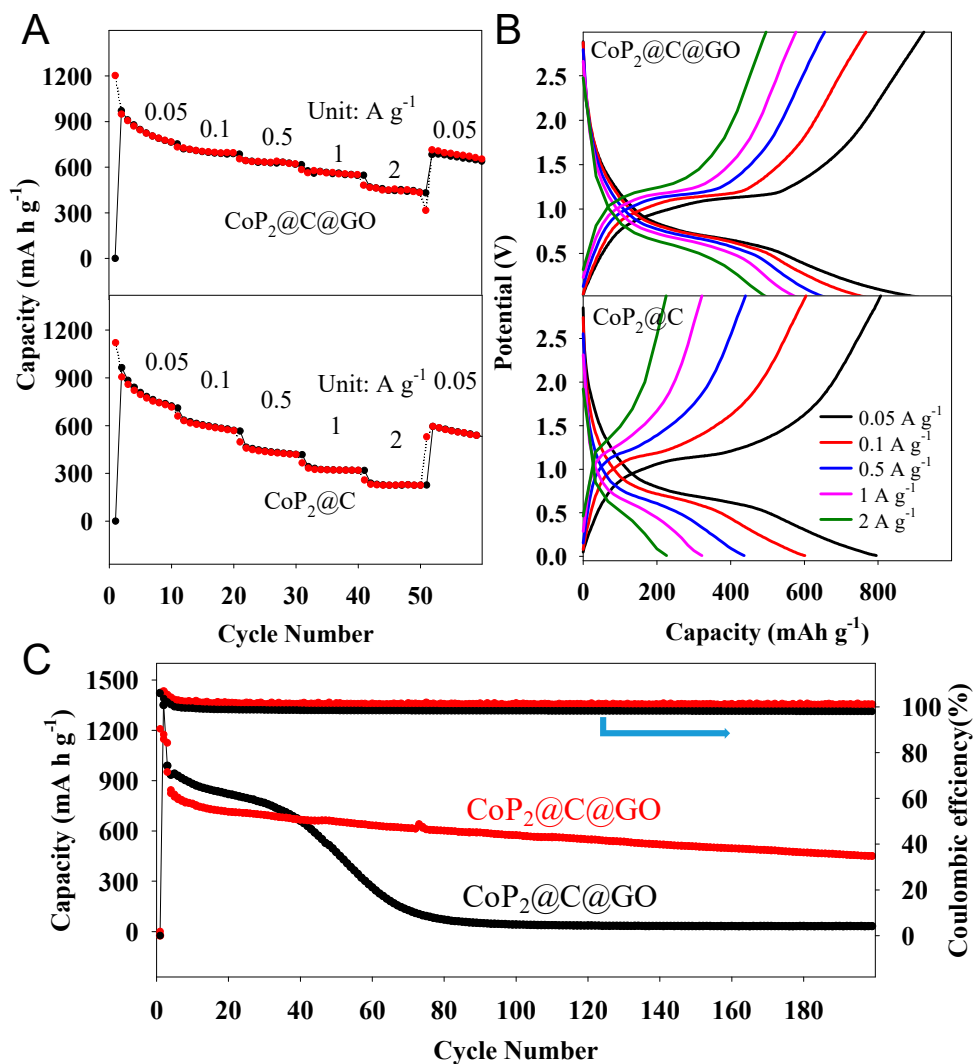

Figure 5. (**A**) Rate performance of the CoP$_2$@C and CoP$_2$@C@GO at increasing current density from 50 mA g^{-1} to 2 A g^{-1}. (**B**) The corresponding charge/discharge profiles at various rates. (**C**) Cycling performance of CoP$_2$@C and CoP$_2$@C@GO arrays at 1 A g^{-1}.

In sharp contrast, CoP$_2$@C delivers a much lower capacity (226 mAh$\cdot$g^{-1}) than CoP$_2$@C@GO. In particular, at a current density of 2 A$\cdot$g^{-1}, it only delivers half the specific capacity of CoP$_2$@C@GO. The improved specific capacity of CoP$_2$@C by GO wrapping could possibly be ascribed to the increased electronic conductivity of the anode materials by GO wrapping. As indicated in earlier studies [19], a coating of a conducting PPy layer alleviates the large volumetric variation and promotes charge transfer kinetics during the lithiation/delithiation process, resulting in enhanced rate performance and cycling performance. The corresponding charge/discharge curves are shown in Figure 5B, where a discharge and charge plateau at 0.55 V and 1.22 V, respectively, is in accordance with that in charging/discharging curves in Figure 4B. It is also observed that both the charge voltage and discharge voltage plateaus remain constant, indicating little variation of polarization with the current density and superior rate capability of CoP$_2$@C enabled by GO decoration.

The cycling stability of $CoP_2@C$ and $CoP_2@C@GO$ as anodes of LIBs was further evaluated by galvanostatic charge/discharge cycling at 1 A·g^{-1} in a voltage range of 0.01–3.0 V (Figure 5C). $CoP_2@C@GO$ nanorod arrays show a specific capacity of about 452 mAh·g^{-1} after 200 cycles and a high Coulombic efficiency near 100% during all 200 cycles. However, the $CoP_2@C$ performs poorly in terms of stability, with only 43 mAh·g^{-1} after 200 cycles. The $CoP_2@C@GO$ exhibits superior reversible capacity and capacity retention to other anode materials for LIBs reported in the literature (Table S1) [46–53]. As demonstrated in a prior report [11], increasing the carbon content offers high electronic conductivity, fast reaction kinetics, structural integrity and thus enhanced capacity of LIBs in cycling.

Figure 6 shows the SEM images of $CoP_2@C$ and $CoP_2@C@GO$ after 200 cycles. The morphology of $CoP_2@C@GO$ remains in shape. However, $CoP_2@C$ shows a lot of agglomeration and collapse of the structure. This indicates that the structure of $CoP_2@C$ was greatly damaged during the insertion and extraction of lithium ions, but the presence of GO can greatly increase the structural integrity of $CoP_2@C$, thereby improving the cycle stability of the material. The changes in particle size for both $CoP_2@C$ and $CoP_2@C@GO$ were assessed before and after cycling using a counting method (Figure S3). The results indicated that prior to the reaction, $CoP_2@C$ had a particle size of approximately 65 nm $\pm$ 8 nm. However, after the reaction during cycling, significant agglomeration occurred, resulting in a larger particle size of about 150 nm $\pm$ 60 nm. In contrast, the particle size of $CoP_2@C@GO$ remained relatively consistent at around 60 nm (from 60 $\pm$ 8 nm to 62 $\pm$ 8 nm). This observation underscores the effectiveness of GO encapsulation in mitigating volume expansion of the anode material during battery charge and discharge cycles and substantial improvement in cycle stability.
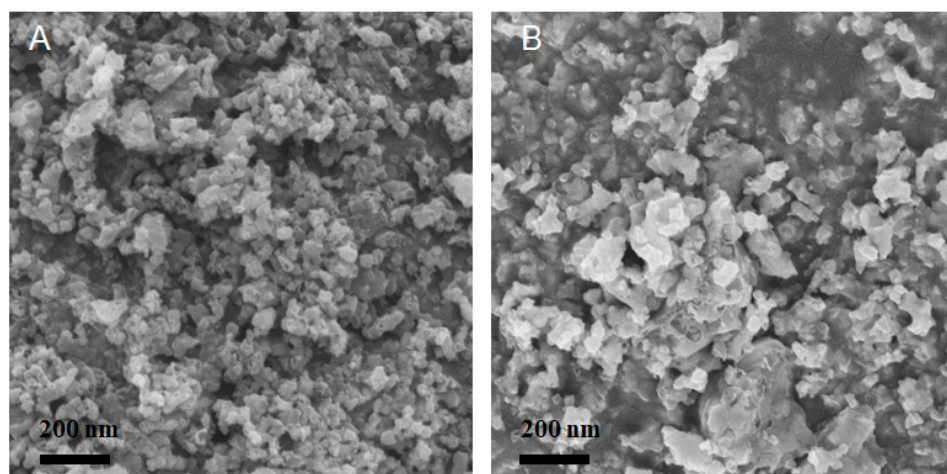

Figure 6. SEM image of (**A**) $CoP_2@C@GO$ and (**B**) $CoP_2@C$ after 200 cycles at 1 A g^{-1}.

To gain further insights into the improved cycling stability of $CoP_2@C$ by GO wrapping, electrochemical impedance spectroscopy (EIS) was utilized as a valuable tool for investigating changes in the conductivity of the prepared electrodes, as illustrated in Figure 7. Each Nyquist plot comprises a distinctive depressed semicircle in the mid- to high-frequency domain, along with a sloping line in the low-frequency region. The diameter of this semicircle is closely associated with the charge transfer resistance (Rct). Notably, the $CoP_2@C@GO$ electrode exhibits a notably smaller Rct than that of the $CoP_2@C$ electrode. This observation highlights the superior charge transfer capability of $CoP_2@C@GO$ electrodes endowed with GO wrapping. This improvement can be attributed to the high electronic conductivity of graphene, which effectively reduces the charge transfer resistance [49]. The enhanced charge transfer kinetics undoubtedly plays a pivotal role in improving the electrochemical performance of $CoP_2@C@GO$ when employed as an anode material of LIBs.

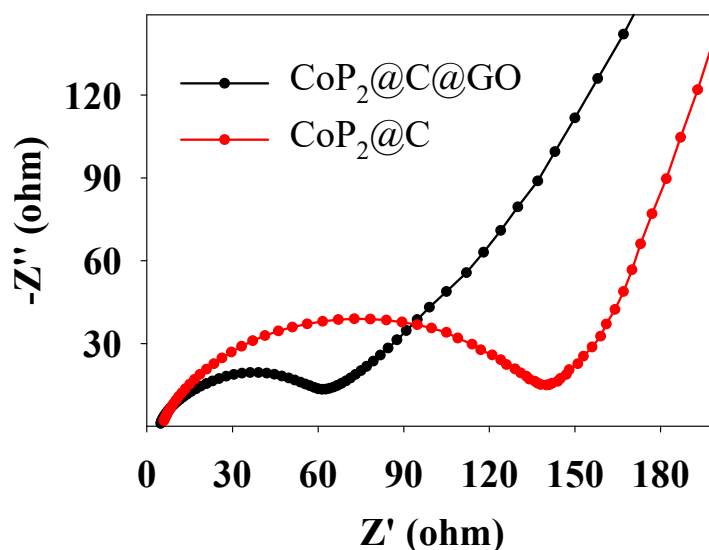**Figure 7.** Nyquist plots for CoP$_2$@C and CoP$_2$@C@GO anodes in the frequency range of 100 kHz–100 mHz.

3. Materials and Methods

3.1. Chemicals

Cobalt nitrate (Co(NO$_3$)$_2$·6H$_2$O, 99%, Damao Chemical Reagents Factory, Tianjin, China), methanol (CH$_3$OH, 99%, DM, Energy Chemical, Beijing, China), 2-methylimidazole (C$_4$H$_6$N$_2$, 99%, Energy Chemical, Beijing, China) and carbon black (Super P, 99%, Timcal, Switzerland) were used. All chemicals were consumed as received. Deionized water was obtained from a Barnstead Nanopure water system (18.2 MΩ·cm).

3.2. Synthesis of ZIF-67

All the chemicals utilized in this study were of analytical grade and were used without the need for further purification. A typical synthesis procedure for ZIF-67 is as follows:

(1) Begin by dispersing 20 mmol of cobaltous nitrate hexahydrate (Co(NO$_3$)$_2$·6H$_2$O equivalent to 5.820 g) in 250 mL of methyl alcohol. This is carried out under vigorous stirring for approximately 5 min, resulting in solution A. (2) In a separate container, dissolve 80 mmol of 2-methylimidazole (equivalent to 6.560 g) in 250 mL of methyl alcohol, yielding solution B. (3) Vigorously shake solution B for several minutes and then carefully pour it into solution A, all while maintaining continuous stirring. (4) As these solutions combine, an immediate color change from pink to a deep purple hue occurs. Allow the combined solution to stir for approximately 1 h. Subsequently, leave the entire solution undisturbed at room temperature for a period of 24 h. (5) The resulting precipitates can be collected through centrifugation. Afterward, wash these precipitates thoroughly with methanol, repeating the process three times. (6) Finally, transfer the washed precipitates to an oven and dry them at 70 °C overnight. This will yield the desired purple ZIF-67 material.

3.3. Synthesis of CoP$_2$@C

The commercial red phosphorus and the ZIF-67 crystal prepared above were completely ground with a mass ratio of 1:1 in a quartz mortar for 1 h. Then, the mixed powder was transferred to a tube furnace, heated to 600 °C with a ramp rate of 2 °C min^{-1} and annealed under an argon atmosphere at 600 °C for 2 h for carbonization of ZIF-67 and phosphorization of Co ions. The obtained products were designated as CoP$_2$@C.

3.4. Synthesis of GO

The synthesis of graphene oxide (GO) was carried out through a modified Hummers method, with the following steps: (1) Begin by combining a mixture of concentrated H$_2$SO4 and H$_3$PO4 in a 400 mL volume, maintaining a ratio of 9:1. (2) Add this mixture to a blend

of graphite (3.0 g) and $KMnO_4$ (18.0 g). Keep the reaction at a constant temperature of 50 °C for a duration of 12 h. (3) After this period, allow it to cool to room temperature. (4) Gradually introduce 230 mL of H_2O into the reaction container. Heat the solution to 98 °C and continue stirring for at least 30 min. (5) Add 500 mL of H_2O into the resulting solution to create a diluted solution. Incorporate 5 mL of H_2O_2 (30%) into this diluted solution. The resulting solution should exhibit a bright yellow color. (6) Wash this solution by subjecting it to three cycles of centrifugation with 5% HCl, followed by rinsing with water. These steps will lead to the production of graphene oxide (GO).

3.5. Synthesis of CoP$_2$@C@GO

CoP_2@C@GO used in this study was prepared as follows. GO and CoP_2@C were first dispersed in 1 M HCl solution, then sonicated for 10 min and stirred for 1 h. The precipitate was collected and washed with water and ethanol using a centrifuge. The product was then dried at 60 °C in air for 12 h. The obtained sample is denoted as CoP_2@C@GO.

3.6. Materials Characterization

(1) X-ray diffraction (XRD) measurements were meticulously conducted using state-of-the-art equipment, namely the Bruker D8 Advance instrument, which hails from Germany. This instrument harnessed the power of Cu-Kα radiation with an exceedingly precise wavelength (λ) of 1.5406 Å. (2) The comprehensive analysis of X-ray photoelectron spectra (XPS) was executed with great precision, employing the cutting-edge Phi X-tool instrument. (3) In the pursuit of a thorough understanding of the samples' morphology, we turned to the capabilities of field-emission scanning electron microscopy (SEM), masterfully performed using the renowned Hitachi S-4800 instrument. (4) For a closer look at the nanoscale structure, high-resolution transmission electron microscopy (HRTEM) was undertaken, with no compromise in quality, thanks to the JEOL JEM-2010 microscope.

3.7. Coin Cell Assembly

A slurry-coating procedure was adopted for the preparation of the working electrode as follows. Firstly, a homogeneous slurry was prepared by mixing CoP_2@C (or CoP_2@C@GO), carbon black (Super P, Timcal) and sodium alginate binder at a mass ratio of 8:1:1, evenly pasted onto a copper foil by applying a film applicator and dried at 70 °C in an electric oven overnight in order to remove the solvent. The mass loading of CoP_2@C (or CoP_2@C@GO) was about 1.1–1.5 mg·cm^{-2} on each electrode.

CR2032-type coin cells were placed in an argon-filled glove box (Vigor-LG2400/750TS, Ltd., Suzhou, China), in which the oxygen and water contents were less than 1 ppm. A Li metal foil, with dimensions of 15.6 mm × 0.45 mm (diameter × thickness) was applied as both counter and reference electrode. A Celgard-2400 film was used as a separator. The recipe of the commercial electrolyte is 1.0 M LiPF$_6$ in a mixed solvent of ethylene carbonate (EC), ethyl methyl carbonate (EMC) and dimethyl carbonate (DMC) at a volume ratio of 1:1:1.

3.8. Electrochemical Measurements

Cyclic voltammetry (CV) and electrochemical impedance spectroscopy (EIS) measurements were conducted on a CHI 660 electrochemical workstation (Shanghai CH Instrument Co., Ltd., Shanghai, China) at room temperature. The galvanostatic charge/discharge measurements were performed on a multichannel battery testing system (CT2001A, LAND).

4. Conclusions

In summary, we successfully prepared CoP_2@C nanomaterials by sequential carbonization and phosphorylation of ZIF-67 and wrapping of GO, which was confirmed by XRD, XPS and TEM. The energy storage capacity of CoP_2@GO as an anode of LIBs was remarkably enhanced by GO wrapping, delivering a capacity of 450 mAh·g^{-1} after 200 cycles

at 1 A g^{-1}. Such improved energy storage performance was ascribed to the improved integrity of the anode materials by GO during charge and discharge processes.

Supplementary Materials: The following supporting information can be downloaded at: https://www.mdpi.com/article/10.3390/electrochem4040031/s1, Figure S1: SEM images of ZIF-67; Figure S2: (A) Full XPS of CoP$_2$@C, high-resolution XPS of (B) N 1s, (C) P 2p, (D) Co of CoP$_2$@C. Figure S3: Size distribution histograms of (A) CoP$_2$@C, (B) CoP$_2$@C@CO with fresh material, (C) CoP$_2$@C and (D) CoP$_2$@C@GO after 200 cycles at 1 A g^{-1}, respectively. Table S1. Electrochemical performance of reported anode materials for LIBs reported in the literature.

Author Contributions: Conceptualization, K.M. and W.Z.; methodology, H.X.; validation, H.X., Z.D. and Z.H.; formal analysis, W.Z.; investigation, W.Z. and K.M.; resources, Q.H. and C.W.; data curation, Z.G.; writing—original draft preparation, W.Z. and K.M.; writing—review and editing, W.Z. and X.K.; supervision, X.K. All authors have read and agreed to the published version of the manuscript.

Funding: This research received no external funding.

Institutional Review Board Statement: Not applicable.

Informed Consent Statement: Not applicable.

Data Availability Statement: The data presented in this study are available on request from the corresponding author.

Conflicts of Interest: The authors declare no conflict of interest.

References

1. Zhang, D.Q.; Ren, J.F.; Li, C.X.; Luo, B.; Wang, L.; Li, Y.Y. An Advanced Design Concept of Mansion-like Freestanding Silicon Anodes with Improved Lithium Storage Performances. *Chin. J. Struct. Chem.* **2022**, *41*, 2205055–2205062. [CrossRef]
2. Lin, J.J.; Zhou, Y.; Wen, J.B.; Si, W.J.; Gao, H.C.; Wang, G.M.; Kang, X.W. Pyrrole derivatives as interlayer modifier of Li-S batteries: Modulation of electrochemical performance by molecular perturbation. *J. Energy Chem.* **2022**, *75*, 164–172. [CrossRef]
3. Liang, Z.L.; Yang, Y.; Li, H.; Liu, L.Y.; Shi, Z.C. Lithium Storage Performance of Hard Carbons Anode Materials Prepared by Different Precursors. *J. Electrochem.* **2021**, *27*, 177–184. [CrossRef]
4. Kim, Y.; Hwang, H.; Yoon, C.S.; Kim, M.G.; Cho, J. Reversible Lithium Intercalation in Teardrop-Shaped Ultrafine SnP$_{0.94}$ Particles: An Anode Material for Lithium-Ion Batteries. *Adv. Mater.* **2007**, *19*, 92–96. [CrossRef]
5. Boyanov, S.; Zitoun, D.; Ménétrier, M.; Jumas, J.C.; Womes, M.; Monconduit, L. Comparison of the Electrochemical Lithiation/Delitiation Mechanisms of FeP$_x$ (*x* = 1, 2, 4) Based Electrodes in Li-Ion Batteries. *J. Phys. Chem. C* **2009**, *113*, 21441–21452. [CrossRef]
6. Hall, J.W.; Membreno, N.; Wu, J.; Celio, H.; Jones, R.A.; Stevenson, K.J. Low-Temperature Synthesis of Amorphous FeP$_2$ and Its Use as Anodes for Li Ion Batteries. *J. Am. Chem. Soc.* **2012**, *134*, 5532–5535. [CrossRef]
7. Park, C.-M.; Sohn, H.-J. Tetragonal Zinc Diphosphide and Its Nanocomposite as an Anode for Lithium Secondary Batteries. *Chem. Mater.* **2008**, *20*, 6319–6324. [CrossRef]
8. Xiang, J.Y.; Wang, X.L.; Zhong, J.; Zhang, D.; Tu, J.P. Enhanced rate capability of multi-layered ordered porous nickel phosphide film as anode for lithium ion batteries. *J. Power Sources* **2011**, *196*, 379–385. [CrossRef]
9. Carenco, S.; Surcin, C.; Morcrette, M.; Larcher, D.; Mézailles, N.; Boissière, C.; Sanchez, C. Improving the Li-Electrochemical Properties of Monodisperse Ni$_2$P Nanoparticles by Self-Generated Carbon Coating. *Chem. Mater.* **2012**, *24*, 688–697. [CrossRef]
10. Cabana, J.; Monconduit, L.; Larcher, D.; Palacín, M.R. Beyond Intercalation-Based Li-Ion Batteries: The State of the Art and Challenges of Electrode Materials Reacting Through Conversion Reactions. *Adv. Mater.* **2010**, *22*, E170–E192. [CrossRef]
11. Kim, S.O.; Manthiram, A. Phosphorus-Rich CuP$_2$ Embedded in Carbon Matrix as a High-Performance Anode for Lithium-Ion Batteries. *ACS Appl. Mater. Interfaces* **2017**, *9*, 16221–16227. [CrossRef]
12. Kwon, H.T.; Kim, J.H.; Jeon, K.J.; Park, C.M. CoxP compounds: Electrochemical conversion/partial recombination reaction and partially disproportionated nanocomposite for Li-ion battery anodes. *RSC Adv.* **2014**, *4*, 43227–43234. [CrossRef]
13. Jiao, G.H.; Gu, Y.; Wang, J.; Wu, D.J.; Tao, S.; Chu, S.Q.; Liu, Y.S.; Qian, B.; Chu, W.S. Porous CoP/C@MCNTs hybrid composite derived from metal-organic frameworks for high-performance lithium-ion batteries. *J. Mater. Sci.* **2019**, *54*, 3273–3283. [CrossRef]
14. Wang, X.X.; Na, Z.L.; Yin, D.M.; Wang, C.L.; Wu, Y.M.; Huang, G.; Wang, L.M. Phytic Acid-Assisted Formation of Hierarchical Porous CoP/C Nanoboxes for Enhanced Lithium Storage and Hydrogen Generation. *ACS Nano* **2018**, *12*, 12238–12246. [CrossRef]
15. Cui, Y.H.; Xue, M.Z.; Fu, Z.W.; Wang, X.L.; Liu, X.J. Nanocrystalline CoP thin film as a new anode material for lithium ion battery. *J. Alloys Compd.* **2013**, *555*, 283–290. [CrossRef]
16. Jiang, J.T.; Zhu, K.; Fang, Y.Z.; Wang, H.Z.; Ye, K.; Yan, J.; Wang, G.L.; Cheng, K.; Zhou, L.M.; Cao, D.X. Coralloidal carbon-encapsulated CoP nanoparticles generated on biomass carbon as a high-rate and stable electrode material for lithium-ion batteries. *J. Colloid Interface Sci.* **2018**, *530*, 579–585. [CrossRef]

17. Chen, M.N.; Zeng, P.Y.; Zhao, Y.Y.; Fang, Z. CoP nanoparticles enwrapped in N-doped carbon nanotubes for high performance lithium-ion battery anodes. *Front. Mater. Sci.* **2018**, *12*, 214–224. [CrossRef]

18. Han, Z.; Wang, B.B.; Liu, X.J.; Wang, G.; Wang, H.; Bai, J.T. Peapod-like one-dimensional (1D) CoP hollow nanorods embedded into graphene networks as an anode material for lithium-ion batteries. *J. Mater. Sci.* **2018**, *53*, 8445–8459. [CrossRef]

19. Liu, Q.; Luo, Y.; Chen, W.L.; Yan, Y.W.; Xue, L.H.; Zhang, W.X. CoP₃@PPy microcubes as anode for lithium-ion batteries with improved cycling and rate performance. *Chem. Eng. J.* **2018**, *347*, 455–461. [CrossRef]

20. Xia, G.; Su, J.; Li, M.; Jiang, P.; Yang, Y.; Chen, Q. A MOF-derived self-template strategy toward cobalt phosphide electrodes with ultralong cycle life and high capacity. *J. Mater. Chem. A* **2017**, *5*, 10321–10327. [CrossRef]

21. Shen, J.H.; Wang, Y.; Yao, Y.F.; Hou, L.; Gu, K.L.; Zhu, Y.H.; Li, C.Z. Flexible Free-Standing Hierarchical Carbon-Coated CoP₂ Nanosheets for High-Performance Lithium-Ion Batteries. *ACS Appl. Energ. Mater.* **2018**, *1*, 7253–7262. [CrossRef]

22. Khatib, R.; Dalverny, A.L.; Saubanère, M.; Gaberscek, M.; Doublet, M.L. Origin of the Voltage Hysteresis in the CoP Conversion Material for Li-Ion Batteries. *J. Phys. Chem. C* **2013**, *117*, 837–849. [CrossRef]

23. Xu, L.; Thompson, C.V. Mechanisms of the cyclic (de)lithiation of RuO₂. *J. Mater. Chem. A* **2020**, *8*, 21872–21881. [CrossRef]

24. Xu, L.; Chon, M.J.; Mills, B.; Thompson, C.V. Mechanical stress and morphology evolution in RuO₂ thin film electrodes during lithiation and delithiation. *J. Power Sources* **2022**, *552*, 232260. [CrossRef]

25. Song, H.R.; Xue, S.D.; Chen, S.M.; Wang, Z.J.; Song, Y.L.; Li, J.W.; Song, Z.B.; Yang, L.Y.; Pan, F. Polymeric Wetting Matrix for a Stable Interface between Solid-state Electrolytes and Li Metal Anode. *Chin. J. Struct. Chem.* **2022**, *41*, 2205048–2205054. [CrossRef]

26. Ma, D.J.; Zhu, Q.L.; Li, X.T.; Gao, H.C.; Wang, X.F.; Kang, X.W.; Tian, Y. Unraveling the Impact of Ether and Carbonate Electrolytes on the Solid-Electrolyte Interface and the Electrochemical Performances of ZnSe@C Core-Shell Composites as Anodes of Lithium-Ion Batteries. *ACS Appl. Mater. Interfaces* **2019**, *11*, 8009–8017. [CrossRef]

27. Gao, H.C.; Ning, S.L.; Zhou, Y.; Men, S.; Kang, X.W. Polyacrylonitrile-induced formation of core-shell carbon nanocages: Enhanced redox kinetics towards polysulfides by confined catalysis in Li-S batteries. *Chem. Eng. J.* **2021**, *408*, 127323. [CrossRef]

28. Yang, J.; Gao, H.C.; Men, S.; Shi, Z.Q.; Lin, Z.; Kang, X.W.; Chen, S.W. CoSe₂ Nanoparticles Encapsulated by N-Doped Carbon Framework Intertwined with Carbon Nanotubes: High-Performance Dual-Role Anode Materials for Both Li- and Na-Ion Batteries. *Adv. Sci.* **2018**, *5*, 1800763. [CrossRef]

29. Men, S.; Zheng, H.; Ma, D.J.; Huang, X.L.; Kang, X.W. Unraveling the stabilization mechanism of solid electrolyte interface on ZnSe by rGO in sodium ion battery. *J. Energy Chem.* **2021**, *54*, 124–130. [CrossRef]

30. Chen, M.; Zhao, J.M.; Sun, C.A.F. High-volumetric-capacity WSe₂ Anode for Potassium-ion Batteries. *Chin. J. Struct. Chem.* **2021**, *40*, 926–932. [CrossRef]

31. Xu, X.J.; Liu, J.; Hu, R.Z.; Liu, J.W.; Ouyang, L.Z.; Zhu, M. Self-Supported CoP Nanorod Arrays Grafted on Stainless Steel as an Advanced Integrated Anode for Stable and Long-Life Lithium-Ion Batteries. *Chem.-Eur. J.* **2017**, *23*, 5198–5204. [CrossRef]

32. Hu, Y.J.; Yin, Y.H.; Zhang, M.; Wu, Z.P.; Shen, Z.R. In-situ Growth of Carbon Nanosheets Intercalated with TiO₂ for Improving Electrochemical Performance and Stability of Lithium-ion Batteries. *Chin. J. Struct. Chem.* **2021**, *40*, 1513–1524. [CrossRef]

33. Chai, S.W.; Xiao, X.; Li, Y.B.; An, C.H. Graphene-Coated 1D MoTe₂ Nanorods as Anode for Enhancing Lithium-Ion Battery Performance. *Chin. J. Struct. Chem.* **2022**, *41*, 2208018–2208024. [CrossRef]

34. Gan, Y.M.; Zhu, J.J.; Zhang, Q.X.; Wang, C.Y.; Guan, L.H.; Zhao, Y. Boosting Stable and Fast Potassium Storage of Iron Sulfide through Rational Yolk-Shell Design and Ni Doping. *Chin. J. Struct. Chem.* **2022**, *41*, 2205030–2205036. [CrossRef]

35. Liu, J.D.Y.; Yu, X.; Bao, J.Z.; Lin, Y.X. A Polyanionic, Quasi-zero-strain and Open-framework K₀.₇₆V₀.₅₅Nb₀.₄₅OPO₄ for Sodium-ion Batteries. *Chin. J. Struct. Chem.* **2021**, *40*, 1631–1638. [CrossRef]

36. Yang, X.; Wang, Z.D.; Fu, Y.R.; Liu, Q.; Xiao, G. Ca₂Nb₂O₇ as a Novel Open-framework Anode Material for Potassium-ion Batteries. *Chin. J. Struct. Chem.* **2021**, *40*, 233–238. [CrossRef]

37. Teng, X.; Niu, Y.; Gong, S.; Liu, X.; Chen, Z. Selective CO₂ Reduction to Formate on Heterostructured Sn/SnO₂ Nanoparticles Promoted by Carbon Layer Networks. *J. Electrochem.* **2022**, *28*, 2108441. [CrossRef]

38. Wu, R.; Wang, D.P.; Zhou, K.; Srikanth, N.; Wei, J.; Chen, Z. Porous cobalt phosphide/graphitic carbon polyhedral hybrid composites for efficient oxygen evolution reactions. *J. Mater. Chem. A* **2016**, *4*, 13742–13745. [CrossRef]

39. Wang, J.-Y.; Tong, X.-F.; Peng, Q.-F.; Guan, Y.-P.; Wang, W.-K.; Wang, A.-B.; Liu, N.-Q.; Huang, Y.-Q. Efficient Interface Enabled by Nano-Hydroxyapatite@Porous Carbon for Lithium-Sulfur Batteries. *J. Electrochem.* **2022**, *28*, 2219008. [CrossRef]

40. Long, X.Y.; Meng, J.Z.; Gu, J.B.; Ling, L.Q.; Li, Q.W.; Liu, N.; Wang, K.W.; Li, Z.Q. Interfacial Engineering of NiFeP/NiFe-LDH Heterojunction for Efficient Overall Water Splitting. *Chin. J. Struct. Chem.* **2022**, *41*, 2204046–2204053. [CrossRef]

41. Li, L.H.; Tian, T.; Cai, Q.R.; Shih, C.J.; Santos, E.J.G. Asymmetric electric field screening in van der Waals heterostructures. *Nat. Commun.* **2018**, *9*, 1271. [CrossRef]

42. Chen, S.; Zheng, S.-S.; Zheng, L.-M.; Zhang, Y.-H.; Wang, Z.-L. Optimized Electrochemical Performance of Si@C Prepared by Hydrothermal Reaction and Glucose Carbon Source. *J. Electrochem.* **2022**, *28*, 2112221. [CrossRef]

43. Yang, D.; Zhu, J.; Rui, X.; Tan, H.; Cai, R.; Hoster, H.E.; Yu, D.Y.W.; Hng, H.H.; Yan, Q. Synthesis of Cobalt Phosphides and Their Application as Anodes for Lithium Ion Batteries. *ACS Appl. Mater. Interfaces* **2013**, *5*, 1093–1099. [CrossRef] [PubMed]

44. Yang, J.; Gao, H.C.; Ma, D.J.; Zou, J.S.; Lin, Z.; Kang, X.W.; Chen, S.W. High-performance Li-Se battery cathode based on CoSe₂-porous carbon composites. *Electrochim. Acta* **2018**, *264*, 341–349. [CrossRef]

45. Jiang, J.; Wang, C.; Li, W.; Yang, Q. One-pot synthesis of carbon-coated Ni₅P₄ nanoparticles and CoP nanorods for high-rate and high-stability lithium-ion batteries. *J. Mater. Chem. A* **2015**, *3*, 23345–23351. [CrossRef]

46. Cai, W.; Yan, C.; Yao, Y.-X.; Xu, L.; Xu, R.; Jiang, L.-L.; Huang, J.-Q.; Zhang, Q. Rapid Lithium Diffusion in Order@Disorder Pathways for Fast-Charging Graphite Anodes. *Small Struct.* **2020**, *1*, 2000010. [CrossRef]

47. Ge, X.; Li, Z.; Yin, L. Metal-organic frameworks derived porous core/shellCoP@C polyhedrons anchored on 3D reduced graphene oxide networks as anode for sodium-ion battery. *Nano Energy* **2017**, *32*, 117–124. [CrossRef]

48. Li, J.; Zhang, T.; Han, C.; Li, H.; Shi, R.; Tong, J.; Li, B. Crystallized lithium titanate nanosheets prepared via spark plasma sintering for ultra-high rate lithium ion batteries. *J. Mater. Chem. A* **2019**, *7*, 455–460. [CrossRef]

49. Li, Z.; Zhang, L.; Ge, X.; Li, C.; Dong, S.; Wang, C.; Yin, L. Core-shell structured CoP/FeP porous microcubes interconnected by reduced graphene oxide as high performance anodes for sodium ion batteries. *Nano Energy* **2017**, *32*, 494–502. [CrossRef]

50. Rhee, D.Y.; Kim, J.; Moon, J.; Park, M.-S. Off-stoichiometric TiO_{2-x}-decorated graphite anode for high-power lithium-ion batteries. *J. Alloys Compd.* **2020**, *843*, 156042. [CrossRef]

51. Von Lim, Y.; Huang, S.; Zhang, Y.; Kong, D.; Wang, Y.; Guo, L.; Zhang, J.; Shi, Y.; Chen, T.P.; Ang, L.K.; et al. Bifunctional porous iron phosphide/carbon nanostructure enabled high-performance sodium-ion battery and hydrogen evolution reaction. *Energ. Storage Mater.* **2018**, *15*, 98–107. [CrossRef]

52. Wang, J.; Yang, Z.; Li, W.; Zhong, X.; Gu, L.; Yu, Y. Nitridation Br-doped $Li_4Ti_5O_{12}$ anode for high rate lithium ion batteries. *J. Power Sources* **2014**, *266*, 323–331. [CrossRef]

53. Zhang, X.-H.; Jiang, R.; Fan, C.-Y.; Xie, D.; Li, B.; Zhang, J.-P.; Wu, X.-L. Engineering All-Purpose Amorphous Carbon Nanotubes with High N/O-Co-Doping Content to Bridge the Alkali-Ion Batteries and Li Metal Batteries. *Small* **2021**, *17*, 2006566. [CrossRef] [PubMed]